



Degree Project in Space Technology

Second cycle, 30 credits

Characterization of the magnetic attitude control limits for low inclination orbits

MATHIS HAMANI

Characterization of the magnetic attitude control limits for low inclination orbits

Mathis Hamani, Aerospace Engineering MSc student
KTH Royal Institute of Technology, Stockholm, Sweden

Abstract— Magnetic attitude control is a widely used spacecraft actuation system as it offers robust, reliable and low power attitude control. As of today, it is primarily used for polar orbits as reduced geomagnetic field variability causes diminished control authority in low-inclination orbits. This paper characterized the operational limits of such systems by identifying key figures of merit (mainly detumbling time and final attitude description) and analyzing their evolution as inclination goes from a quasi polar sun-synchronous orbit to an equatorial orbit. If the use of magnetic attitude control was possible at lower inclination orbits, this would greatly help missions at such orbits by having a reliable and robust attitude control solution. High-fidelity simulations with variability of initial conditions (initial orbital parameters, residual magnetic moment, etc.) were ran in order to obtain general results. In addition, a theoretical stability analysis was completed in order to understand the origin of the degradation of control performance. This study showed that magnetic attitude control can be used for detumbling in low Earth orbit with an inclination as low as 35° in less than 2 orbits. Moreover, it was shown that the final attitude is always with the axis of spin close the orbit normal (deviation always lower than 45°). This work provided design guidelines for future Cubesat missions in low-inclination orbits, highlighting where magnetic-only control remains viable and where supplemental actuation (e.g., thrusters, reaction wheels) might become necessary.

Sammanfattning— Magnetisk attitydreglering är ett vanligt förekommande manövreringssystem för rymdfarkoster, eftersom det erbjuder robust, tillförlitlig och energisnål attitydreglering. I dagsläget används det främst för polära omloppsbanor, eftersom den minskade variationen i det geomagnetiska fältet leder till försämrade styrförmåga vid banor med låg inklinations. Denna artikel karakteriserar de operativa gränserna för sådana system genom att identifiera viktiga prestationsmått (huvudsakligen inbromsningstid och slutlig attitydsbeskrivning) samt analysera hur dessa utvecklas när inklinationen går från en kvasi-polär solsynkron bana till en ekvatoriell bana. Om magnetisk attitydreglering vore möjlig vid lägre inklinationer skulle detta i hög grad gynna uppdrag i sådana omloppsbanor genom att erbjuda en tillförlitlig och robust lösning för attitydreglering. Numeriska simuleringar med variation av initiala förhållanden (initiala omloppsbaneparametrar, kvarvarande magnetiskt moment, m.m.) genomfördes för att erhålla generella resultat. Dessutom genomfördes en teoretisk stabilitetsanalys för att förstå ursprunget till försämringen av reglerprestanda. Studien visade att magnetisk attitydreglering kan användas för avbromsning i låga jordomloppsbanor med en inklinations så låg som 35 grader, på mindre än 2 varv. Vidare visades att den slutliga attityden alltid är sådan att rotationsaxeln ligger nära banans normalvektor (avvikelsen är alltid mindre än 45 grader).

Detta arbete tillhandahöll riktlinjer för framtida CubeSat-uppdrag i låg-inklinationsbanor, och belyste var magnetisk styrning ensam förblir genomförbart och var kompletterande manöverdon (t.ex. manövreraketer och reaktionshjul) kan bli nödvändig.

Index Terms— Spacecraft attitude control, low-inclination orbits, magnetic actuation, Cubesat dynamics, geomagnetic field modeling, orbital perturbations, IGRF, attitude stabilization, bDot, biased bDot

LIST OF ABBREVIATIONS

AOCS	Attitude and Orbit Control System
ASM	Acquisition and Safe Mode
CNES	Centre National d'Études Spatiales (National Center for Space Studies), the French space agency
COM	Center Of Mass
ECI	Earth Centered Inertial
GCRF	Galactic Celestial Reference Frame
IERS	International Earth Rotation and Reference Systems Service
ITRF	International Terrestrial Reference Frame
LEO	Low Earth Orbit
MTQ	MagneTorQuer
P2P	Peak To Peak
RAAN	Right Ascension of the Ascending Node
RCS	Reaction Control Thruster
s.t.	such that
SSO	Sun-Synchronous Orbit
w.r.t.	with respect to

NOMENCLATURE

C	satellite COM
M	mean anomaly
N	total number of simulations
S	set of potentially stable trajectories
S'	set of stable trajectories
T	simulation time
T_{orbit}	orbital period
$V(\omega)$	Lyapunov candidate function
Ω	RAAN
$\bar{\epsilon}$	mean value during last whole orbit of simulation of angular velocity error to setpoint
B	Earth's magnetic field
F_{ext}	vector of external forces acting on satellite
H_A	satellite angular momentum at point A
I	satellite inertia tensor at COM
I_3	3×3 identity matrix

K	control gain matrix
L_{GG}	gravity gradient torque
L_{MAG}	magnetic disturbance torque
$L_{ext,A}$	external torques acting on satellite at point A
Ω_{MAG}	rotation vector of magnetic field direction
Ω_{bias}	angular velocity setpoint
ω	satellite angular velocity
ω_{init}	initial angular velocity
ε	angular velocity error to setpoint
a_c	satellite acceleration of COM
b	direction of magnetic field
e	Euler axis of rotation
m	magnetic moment
m_{Res}	residual magnetic moment
n	surface normal
q	attitude quaternion
r	radial vector from Earth's COM to C
s	Sun direction vector
t	surface tangent
δ	pointing error
$\left. \frac{d}{dt} \right _B$	time derivative w.r.t. body frame
$\left. \frac{d}{dt} \right _I$	time derivative w.r.t. inertial frame
$d\mathbf{f}_{absorbed}$	absorbed component of solar radiation pressure
$d\mathbf{f}_{diffused}$	diffused component of solar radiation pressure
$d\mathbf{f}_{specular}$	specular component of solar radiation pressure
$d\mathbf{f}_n, d\mathbf{f}_t$	normal and tangential components of aerodynamic pressure
μ	Earth's gravitational parameter
ω	argument of perigee
XSat	satellite x axis
YSat	satellite y axis
ZSat	satellite z axis
θ	rotation angle around Euler axis
a	semi-major axis
e	orbit eccentricity
i	orbit inclination
k	control gain
m	satellite mass
$t_{conv}, t_{conv, \delta}$	angular velocity and attitude convergence times
x_c, y_c, z_c	COM position in GCRF Cartesian coordinates

Contents

I	INTRODUCTION	3
II	METHOD	3
II.A	Method Outline	3
II.B	System modelization	4
II.B.1	Reference frames	4
II.B.2	Attitude parametrization	4
II.C	Equations of motion	5
II.C.1	Kinematics differential equation	5
II.C.2	Translational equation of motion	5
II.C.3	Rotational equation of motion	5
II.C.4	Disturbance torques and forces	5
II.D	Magnetic control	6
II.D.1	bDot control law	6
II.D.2	Biased bDot control law	7
II.D.3	Stability analysis of the bDot control law	7
II.D.4	Discussion on neglecting the magnetic field time derivative	7
II.D.5	Stability analysis of the biased bDot control law	8
II.E	Simulation settings	8
II.E.1	Fixed simulation settings	8
II.E.2	Swept parameters	9
II.E.3	Randomized parameters	9
II.F	Derivation of results	9
II.F.1	Convergence time	9
II.F.2	Pointing error between two vectors	9
II.F.3	Convergence time of pointing error	10
II.F.4	Convergence diagram	10
III	RESULTS	10
III.A	Simulation parameter sweep	10
III.A.1	Convergence time	10
III.A.2	Mean angular velocity error to setpoint	10
III.A.3	Peak to peak of angular velocity error to setpoint	10
III.A.4	Mean pointing error of ZSat axis w.r.t. orbit normal	11
III.A.5	Convergence time of pointing error of ZSat axis w.r.t. orbit normal	11
III.A.6	Actuator saturation	11
III.A.7	Convergence diagram	11
III.A.8	Convergence time results grouped by other initial conditions	12
III.A.9	Mean pointing error of ZSat axis w.r.t. orbit normal grouped by residual magnetic moment	13
III.B	Single simulation study	14
III.B.1	Traces of B and ZSat axis	14
III.B.2	External torques	15
III.B.3	Metastable state at low inclination orbits	16
IV	DISCUSSION	17
IV.A	Simulation parameter sweep	17
IV.A.1	Convergence time	17

IV.A.2 Mean angular velocity error to setpoint	17
IV.A.3 Peak to peak of angular velocity error to setpoint	17
IV.A.4 Mean pointing error of ZSat axis w.r.t. orbit normal	17
IV.A.5 Convergence time of pointing error of ZSat axis w.r.t. orbit normal	18
IV.A.6 Actuator saturation	18
IV.A.7 Convergence diagram	18
IV.A.8 Convergence time grouped by other initial conditions	18
IV.A.9 Mean pointing error of ZSat axis w.r.t. orbit normal grouped by residual magnetic moment	18
IV.B Single simulation study	19
IV.B.1 Traces of B and ZSat axis	19
IV.B.2 External torques	19
IV.B.3 Metastable state at low inclination orbits	19
IV.C Study limitations	19
V CONCLUSION	19
APPENDIX	20
ACKNOWLEDGMENT	20
References	21

I. INTRODUCTION

Magnetorquers are a very popular solution for attitude control as they are robust, low power, lightweight and do not suffer from fuel limitations or saturation issues unlike other attitude control systems (Reaction Control Thruster (RCS), reaction wheels). However, they offer poor performance compared to these technologies. Thus, they are primarily used in cases where robustness is favored over performance, such as in Acquisition and Safe Mode (ASM), to detumble satellites, point the solar arrays towards the Sun, and for reaction wheel desaturation. Magnetic attitude control works by using Earth’s magnetic field to produce a torque on the satellite. Nevertheless, this torque cannot be obtained in the direction of the magnetic field, posing challenges in low-inclination orbits where this direction is nearly inertial. This limitation significantly reduces control authority around one axis, restricting the use of magnetorquers to polar orbits where the magnetic field direction varies considerably along the trajectory of the satellite.

Therefore, the goal of this study was to quantify the limits of magnetic attitude control for low inclination orbits by defining key figures of merit (FOM) and tracking their evolution as the orbit went from polar to equatorial. Of course, this problem did not depend on one single factor, as satellite attitude and trajectory dynamics are subjected to a great many of external and internal perturbations (disturbance torques and forces, sensor noise and biases, controller settings, satellite configuration, etc.).

To this end, the study mainly focused on a multi-parameter sweep of initial conditions, including orbit inclination, initial angular velocity, and other relevant parameters. Each unique combination of initial conditions led to a distinct simulation. The simulations were conducted using a high-fidelity Cubesat model developed at CNES, which incorporated detailed dynamics, environmental disturbance models (e.g., aerodynamic pressure, solar radiation pressure, gravity gradient and magnetic torque due to residual magnetic moment). Additionally, the model integrated the IGRF Earth magnetic field model for accurate geomagnetic field representation and accounted for orbital perturbations due to Earth’s geometry (e.g., oblateness and higher spherical harmonics) to ensure realistic attitude control performance evaluation.

Complementing the simulations, a theoretical stability analysis of the magnetorquer control law was conducted in order to have a better understanding of the system dynamics. This analysis primarily focused on Lyapunov function analysis and examined common control laws such as bDot and biased bDot, which are widely used in magnetic attitude control solutions.

II. METHOD

A. Method Outline

In order to study this question, the method is organized in the following way.

- A theoretical study is conducted to understand the principles of magnetic attitude control and its limitations. The system modelization and dynamics are detailed followed by a stability analysis of this type of control, especially the bDot and biased bDot control laws, which are widely used for spacecraft detumbling (II.B).
- Then, the multi-parameter sweep and simulation settings are detailed (II.E).

B. System modelization

The satellite is modeled as a rigid body subjected to external forces and torques. Its mass and geometry are based on a 3U Cubesat model developed at CNES.

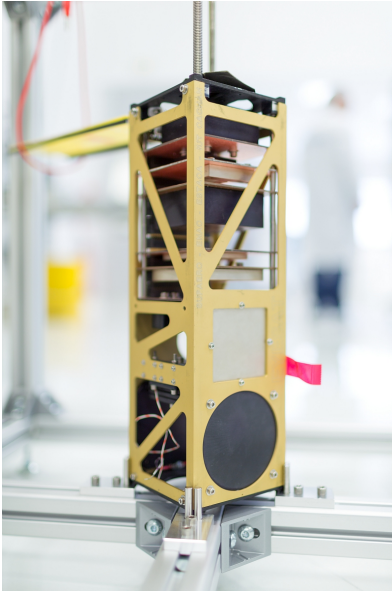


Fig. 1: A 3U Cubesat on its integration test bed.
Credit : ©CNES/LE BRAS Gwenewan, 2018

The equations describing its attitude and motion are described in section II.C.

1. Reference frames

Several reference frames are used in this study, they are defined below :

GCRF

The Galactic Celestial Reference Frame (GCRF) is an Earth-centered inertial (ECI) frame. These axes do not rotate with Earth and are treated as inertial for spacecraft dynamics.

- Origin: Earth's center of mass.
- $+X$: Directed toward the mean equinox of J2000.0, i.e., the intersection of Earth's equatorial plane with the ecliptic at the reference epoch.
- $+Z$: Aligned with Earth's mean rotation axis at J2000.0 (north celestial pole).

- $+Y$: Right-handed completion, 90° east of $+X$.

This reference frame is considered the inertial frame \mathcal{I} in this paper.

ITRF

The International Terrestrial Reference Frame (ITRF) is an Earth-fixed frame that co-rotates with the planet.

- Origin: Earth's center of mass (including oceans and atmosphere).
- $+Z$: Aligned with the International Reference Pole (IRP).
- $+X$: Lies in the equatorial plane and points toward the IERS Reference Meridian, passing through the Greenwich meridian (0° longitude).
- $+Y$: Right-handed completion, 90° east of $+X$.

This reference frame is noted \mathcal{E} in this paper.

BODY-FIXED The body fixed frame, noted \mathcal{B} , is a reference frame rigidly attached to the body.

- Origin: Rigid body's Center Of Mass (COM)
- $+X$: Going from solar panels base along one solar panel axis
- $+Y$: Completes the base
- $+Z$: Along longitudinal axis of satellite, facing away from solar panels

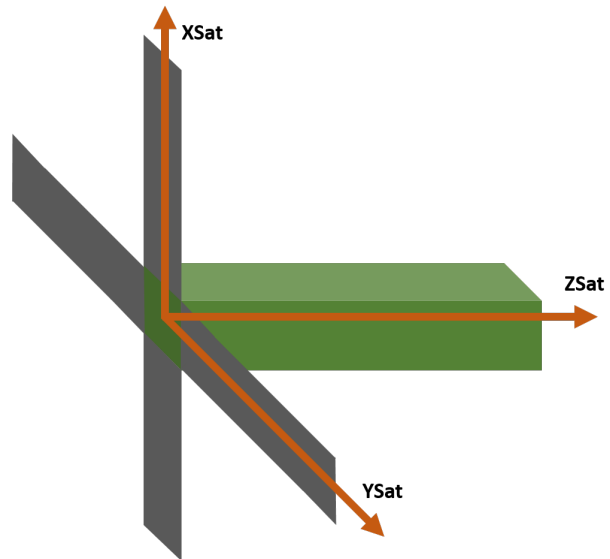


Fig. 2: Body fixed reference frame axes

2. Attitude parametrization

Quaternions are chosen in this study as attitude parameters since they are non singular and broadly used in literature and industry for their linear differential equations and suitability for estimators (e.g. the Kalman filter). The attitude quaternion will be the rotation quaternion from the inertial frame \mathcal{I} to the body-fixed frame \mathcal{B} . The notation is based on [1].

$$\mathbf{q} = \begin{pmatrix} q_0 \\ q_1 \\ q_2 \\ q_3 \end{pmatrix} = \begin{pmatrix} \cos \theta/2 \\ \mathbf{e} \sin \theta/2 \end{pmatrix} \quad (1)$$

with \mathbf{e} the unit vector of the rotation axis and θ the rotation angle around that axis.

The angular velocity of the \mathcal{B} frame w.r.t. the \mathcal{I} frame is noted :

$$\boldsymbol{\omega} = \begin{pmatrix} \omega_1 \\ \omega_2 \\ \omega_3 \end{pmatrix} \quad (2)$$

C. Equations of motion

1. Kinematics differential equation

Using quaternions as the attitude description parameters, we get the following differential equation linking the attitude to the angular velocity, [1] :

$$\begin{pmatrix} \dot{q}_0 \\ \dot{q}_1 \\ \dot{q}_2 \\ \dot{q}_3 \end{pmatrix} = \frac{1}{2} B(\mathbf{q}) \begin{pmatrix} \omega_1 \\ \omega_2 \\ \omega_3 \end{pmatrix} \quad (3)$$

with,

$$B(\mathbf{q}) = \begin{pmatrix} q_0 & -q_1 & -q_2 & -q_3 \\ q_1 & q_0 & -q_3 & q_2 \\ q_2 & q_3 & q_0 & -q_1 \\ q_3 & -q_2 & q_1 & q_0 \end{pmatrix}$$

2. Translational equation of motion

The translational equation of motion for a rigid body is:

$$m \frac{d\mathbf{a}_c}{dt} \Big|_{\mathcal{I}} = \mathbf{F}_{\text{ext}} \quad (4)$$

with,

- C COM,
- \mathbf{a}_c rigid body COM acceleration,
- m body mass,
- \mathbf{F}_{ext} sum of all external forces,
- \mathcal{I} the inertial frame

This leads to, in Cartesian coordinates :

$$\begin{aligned} m\ddot{x}_c &= F_{\text{ext},x} \\ m\ddot{y}_c &= F_{\text{ext},y} \\ m\ddot{z}_c &= F_{\text{ext},z} \end{aligned} \quad (5)$$

with,

- x_c position of C along the x -axis,
- y_c position of C along the y -axis,
- z_c position of C along the z -axis

3. Rotational equation of motion

The following calculations were based on [1]. The rotational equation of motion for a rigid body is, for a given point A:

$$\frac{d\mathbf{H}_A}{dt} \Big|_{\mathcal{I}} = \mathbf{L}_{\text{ext},A} \quad (6)$$

with,

- \mathbf{H}_A rigid body angular momentum about point A
- $\mathbf{L}_{\text{ext},A}$ sum of all external torques about point A
- \mathcal{I} the inertial frame

This yields, taking this equation at the rigid body COM :

$$\begin{aligned} \frac{d\mathbf{H}_c}{dt} \Big|_{\mathcal{I}} &= \mathbf{L}_{\text{ext},c} \\ \frac{d(\mathbf{I}\boldsymbol{\omega})}{dt} \Big|_{\mathcal{I}} &= \mathbf{L}_{\text{ext},c} \\ \frac{d(\mathbf{I}\boldsymbol{\omega})}{dt} \Big|_{\mathcal{B}} + \boldsymbol{\omega} \times \mathbf{I}\boldsymbol{\omega} &= \mathbf{L}_{\text{ext},c} \end{aligned}$$

Thus, as \mathbf{I} is constant in the body frame,

$$\mathbf{I} \frac{d\boldsymbol{\omega}}{dt} \Big|_{\mathcal{B}} = -\boldsymbol{\omega} \times \mathbf{I}\boldsymbol{\omega} + \mathbf{L}_{\text{ext},c} \quad (7)$$

with,

- \mathcal{I} the body inertia tensor at COM
- $\boldsymbol{\omega}$ the body angular velocity
- \mathcal{B} the body-fixed frame

4. Disturbance torques and forces

There are four disturbance sources which can impact attitude and trajectory. Their expressions were obtained from [2].

a. Gravity gradient torque

Gravity gradient torque comes from the non-uniformity of Earth's gravitational field, causing a differential force across a satellite's structure that induces rotational motion.

$$\mathbf{L}_{\text{GG}} = \frac{3\mu}{r^5} \mathbf{r} \times \mathbf{I}\mathbf{r} \quad (8)$$

with,

- μ Earth's gravitational parameter
- \mathbf{r} radial vector going the Earth's COM to the satellite's COM
- $r = \|\mathbf{r}\|$
- \mathbf{I} satellite's inertia tensor

b. Magnetic torque

The torque applied by an external magnetic field \mathbf{B} on a system having a magnetic moment \mathbf{m} is

$$\mathbf{L}_{\text{MAG}} = \mathbf{m} \times \mathbf{B} \quad (9)$$

Typically, the satellite's internal electrical circuits and permanent magnetization of materials generate an unwanted residual magnetic moment that interacts with Earth's magnetic field, producing disturbance torque.

c. Aerodynamic pressure

Aerodynamic pressure arises from the interaction of a satellite's surface with the residual atmospheric particles, generating forces that can affect its attitude and trajectory. The normal and tangential infinitesimal forces acting on a local surface are respectively

$$\begin{aligned} d\mathbf{f}_n &= \frac{1}{2}\rho V^2 C_N dA \cos^2 \alpha \mathbf{n} \\ d\mathbf{f}_t &= \frac{1}{2}\rho V^2 C_T dA \sin \alpha \cos \alpha \mathbf{t} \end{aligned} \quad (10)$$

with,

- ρ atmosphere density
- V satellite speed w.r.t. airflow
- C_N satellite local surface normal coefficient
- C_T satellite local surface tangential coefficient
- dA infinitesimal area
- α : local surface angle of attack
- \mathbf{n} normal vector of local surface
- \mathbf{t} tangent vector of local surface in the direction of the airflow

d. Solar radiation pressure

Solar radiation pressure results from the momentum transfer of photons from the Sun impacting a satellite's surface, exerting a force that can influence its attitude and trajectory. The absorbed, specular and diffused infinitesimal forces acting on a local surface are respectively

$$\begin{aligned} d\mathbf{f}_{\text{absorbed}} &= -PC_a \cos \theta dA \mathbf{s} \\ d\mathbf{f}_{\text{specular}} &= -2PC_s \cos^2 \theta dA \mathbf{n} \\ d\mathbf{f}_{\text{diffused}} &= -PC_d \cos \theta dA \left(\frac{2}{3} \mathbf{n} + \mathbf{s} \right) \end{aligned} \quad (11)$$

with,

- P Solar radiation pressure
- C_a absorption coefficient
- C_s specular reflection coefficient
- C_d diffused reflection coefficient
- θ angle between \mathbf{s} and \mathbf{n}
- dA infinitesimal area
- \mathbf{s} unit vector going from satellite to Sun
- \mathbf{n} normal vector of local surface

For solar radiation and aerodynamic pressures, the point where the force is applied is not necessarily the COM, thus, there might a torque applied by that force. The centers of pressure and overall torques are computed using an external software.

D. Magnetic control

Magnetic control works by creating a magnetic moment, usually with solenoids, and use the Earth magnetic field to apply a torque on the satellite, as stated by (9).

1. bDot control law

The most common magnetic control law used for detumbling is the bDot law, the control moment is

$$\mathbf{m} = -k \frac{\dot{\mathbf{b}}}{\|\mathbf{B}\|} \quad (12)$$

With,

- \mathbf{B} the Earth's magnetic field
- $\mathbf{b} = \frac{\mathbf{B}}{\|\mathbf{B}\|}$ the magnetic field direction
- k the control gain

Here, the dot means taking the time derivative with respect to the body frame $\dot{\mathbf{b}} = \left. \frac{d\mathbf{b}}{dt} \right|_{\mathcal{B}}$

An alternative common expression for the control moment directly accounts for the fact that the component aligned with the magnetic field direction is ineffective due to the nature of the cross product :

$$\mathbf{m} = \mathbf{b} \times \left(-k \frac{\dot{\mathbf{b}}}{\|\mathbf{B}\|} \times \mathbf{b} \right) \quad (13)$$

See justification in the appendix V..0.b.

Thus, using (9), the torque is :

$$\begin{aligned} \mathbf{L}_{\text{MAG}} &= -k \frac{\dot{\mathbf{b}}}{\|\mathbf{B}\|} \times \mathbf{B} \\ &= -k \dot{\mathbf{b}} \times \mathbf{b} \end{aligned} \quad (14)$$

Using the transport theorem,

$$\begin{aligned} \dot{\mathbf{b}} &= \left. \frac{d\mathbf{b}}{dt} \right|_{\mathcal{B}} \\ &= \left. \frac{d\mathbf{b}}{dt} \right|_{\mathcal{I}} - \boldsymbol{\omega} \times \mathbf{b} \end{aligned}$$

Now, assuming that the magnetic field direction is inertial or that $\left. \frac{d\mathbf{b}}{dt} \right|_{\mathcal{I}}$ is negligible w.r.t. the second term (these assumptions are discussed later in II.D.4) :

$$\begin{aligned} \mathbf{L}_{\text{MAG}} &= k (\boldsymbol{\omega} \times \mathbf{b}) \times \mathbf{b} \\ &= k ((\boldsymbol{\omega} \cdot \mathbf{b}) \mathbf{b} - \boldsymbol{\omega}) \\ &= -k (\boldsymbol{\omega} - \mathbf{b} (\mathbf{b} \cdot \boldsymbol{\omega})) \\ \mathbf{L}_{\text{MAG}} &= -k [\mathbf{I}_3 - \mathbf{b}\mathbf{b}^T] \boldsymbol{\omega} \end{aligned} \quad (15)$$

which corresponds to the result found in [3], [4]. Thus, derivating \mathbf{b} provides an estimate of the satellite's angular velocity. This leads to a control law that approximates a proportional feedback loop. This highlights the key advantage of the bDot law: the only sensor required to estimate the angular velocity is a magnetometer.

However, since the matrix $[I_3 - \mathbf{b}\mathbf{b}^T]$ is an orthogonal projector w.r.t. \mathbf{b} , no torque can be applied in the direction of the magnetic field. This qualitatively underlines the issues which appear with this kind of control.

2. Biased bDot control law

The control law is very similar to the bDot one :

$$\mathbf{m} = -\frac{k}{\|\mathbf{B}\|} (\dot{\mathbf{b}} + \boldsymbol{\Omega}_{\text{bias}} \times \mathbf{b}) \quad (16)$$

with, $\boldsymbol{\Omega}_{\text{bias}}$ the angular velocity setpoint.

A non zero $\boldsymbol{\Omega}_{\text{bias}}$ provides gyroscopic stiffness, which increases robustness of the spinning axis pointing when subjected to external torques.

This leads to,

$$\mathbf{L}_{\text{MAG}} = -k \left(\left. \frac{d\mathbf{b}}{dt} \right|_{\mathcal{I}} + (\boldsymbol{\Omega}_{\text{bias}} - \boldsymbol{\omega}) \times \mathbf{b} \right) \times \mathbf{b}$$

Still neglecting $\left. \frac{d\mathbf{b}}{dt} \right|_{\mathcal{I}}$

$$\mathbf{L}_{\text{MAG}} = -k [I_3 - \mathbf{b}\mathbf{b}^T] \tilde{\boldsymbol{\omega}} \quad (17)$$

with, $\tilde{\boldsymbol{\omega}} = (\boldsymbol{\omega} - \boldsymbol{\Omega}_{\text{bias}})$

Similarly, an almost proportional feedback loop to the setpoint $\boldsymbol{\Omega}_{\text{bias}}$ is obtained, with the same limitations as in Eq. (15).

3. Stability analysis of the bDot control law

Let us take the following Lyapunov candidate function

$$V(\boldsymbol{\omega}) = \frac{1}{2} \boldsymbol{\omega}^T I \boldsymbol{\omega} \quad (18)$$

with its derivative

$$\dot{V}(\boldsymbol{\omega}) = \frac{1}{2} \left(\dot{\boldsymbol{\omega}}^T I \boldsymbol{\omega} + \boldsymbol{\omega}^T (I \dot{\boldsymbol{\omega}}) \right) \quad (19)$$

where the dot here is the time derivative w.r.t. the body frame, and since V is a scalar, $\dot{V}^T = \dot{V} \implies \dot{\boldsymbol{\omega}}^T I \boldsymbol{\omega} = \boldsymbol{\omega}^T I \dot{\boldsymbol{\omega}}$, thus :

$$\begin{aligned} \dot{V}(\boldsymbol{\omega}) &= \boldsymbol{\omega}^T I \dot{\boldsymbol{\omega}} \\ &= \boldsymbol{\omega}^T I \left(\left. \frac{d\boldsymbol{\omega}}{dt} \right|_{\mathcal{I}} - \boldsymbol{\omega} \times \boldsymbol{\omega} \right) \\ &= \boldsymbol{\omega}^T \mathbf{L}_{\text{MAG}} \\ \dot{V}(\boldsymbol{\omega}) &= -k \boldsymbol{\omega}^T [I_3 - \mathbf{b}\mathbf{b}^T] \boldsymbol{\omega} \leq 0 \end{aligned} \quad (20)$$

V is positive definite, of class C^1 and \dot{V} is negative semi-definite, so $\boldsymbol{\omega} = 0$ is a stable equilibrium point. LaSalle's invariance principle states that the set of all stable trajectories is the largest set of invariant trajectories S' contained within the set

$$\begin{aligned} S &= \{\boldsymbol{\omega}, \dot{V}(\boldsymbol{\omega}) = 0\} \\ &= \{\boldsymbol{\omega} // \mathbf{b}\} \end{aligned}$$

That is, the configuration where $\boldsymbol{\omega}$ is aligned with \mathbf{b} is also potentially stable. In addition, [3]

shows that $\boldsymbol{\omega} = \mathbf{0}$ is a globally asymptotically stable equilibrium in the case where B varies sufficiently in direction over time. A similar analysis is done in (II.D.5).

However, this analysis relies on the assumption that $\left. \frac{d\mathbf{b}}{dt} \right|_{\mathcal{I}} \approx \mathbf{0}$. The validity of this hypothesis is discussed below in the next section.

4. Discussion on neglecting the magnetic field time derivative

The magnetic field \mathbf{B} is a vector field of the form $\mathbf{B}(\mathbf{r}, t)$, with \mathbf{r} the position at which the field is evaluated and t the time. The field experienced by the satellite is therefore the field at the position $\mathbf{r}_s(t)$ of the satellite $\mathbf{B}(\mathbf{r}_s(t), t)$. Therefore, by applying the chain rule, the total derivative of the magnetic field seen by the satellite is,

$$\begin{aligned} \left. \frac{d\mathbf{B}(\mathbf{r}_s(t), t)}{dt} \right|_{\mathcal{I}} &= \frac{dx}{dt} \frac{\partial \mathbf{B}}{\partial x} + \frac{dy}{dt} \frac{\partial \mathbf{B}}{\partial y} \\ &\quad + \frac{dz}{dt} \frac{\partial \mathbf{B}}{\partial z} + \frac{\partial \mathbf{B}}{\partial t} \Big|_{\mathcal{I}} \end{aligned} \quad (21)$$

Assuming that \mathbf{B} is independent of time at an inertial point (i.e. $\left. \frac{\partial \mathbf{B}}{\partial t} \right|_{\mathcal{I}} = \mathbf{0}$):

$$\begin{aligned} \left. \frac{d\mathbf{B}(\mathbf{r}_s(t), t)}{dt} \right|_{\mathcal{I}} &= v_x \frac{\partial \mathbf{B}}{\partial x} + v_y \frac{\partial \mathbf{B}}{\partial y} + v_z \frac{\partial \mathbf{B}}{\partial z} \\ &= (\mathbf{v} \cdot \nabla) \mathbf{B} \end{aligned} \quad (22)$$

with ∇ the gradient operator and $\mathbf{v} = (v_x, v_y, v_z)$ the velocity of the satellite in the inertial frame. This term is similar to the ‘‘convective term’’ of the Navier-Stokes equation, which can be seen as the variation of the magnetic field along the satellite's trajectory. Neglecting this term in front of $\boldsymbol{\omega} \times \mathbf{B}$ is to be discussed.

Let us now consider the possibility of writing this term as a ‘‘magnetic field rotation’’. That is, expressing it in the form $\boldsymbol{\Omega}_{\text{MAG}} \times \mathbf{B}$, which would allow it to be associated with the term $\boldsymbol{\omega} \times \mathbf{B}$ and would reveal the tracking of $\boldsymbol{\omega}$ on $\boldsymbol{\Omega}_{\text{MAG}}$. We are therefore looking for $\boldsymbol{\Omega}_{\text{MAG}}$ such that:

$$(\mathbf{v} \cdot \nabla) \mathbf{B} = \boldsymbol{\Omega}_{\text{MAG}} \times \mathbf{B} \quad (23)$$

We see well that by the properties of the vector product, it is not possible unless $(\mathbf{v} \cdot \nabla) \mathbf{B} \perp \mathbf{B}$. Let us study this configuration:

$$((\mathbf{v} \cdot \nabla) \mathbf{B}) \cdot \mathbf{B} = \frac{1}{2} (\mathbf{v} \cdot \nabla) (\mathbf{B} \cdot \mathbf{B}) = (\mathbf{v} \cdot \nabla) \|\mathbf{B}\|^2 \quad (24)$$

Therefore, these two vectors are orthogonal if and only if the norm of \mathbf{B} is constant along the satellite's trajectory. Let us assume $\|\mathbf{B}\|$ to be constant $\forall \mathbf{r}, t$. Therefore, to find $\boldsymbol{\Omega}_{\text{MAG}}$, we need to find the vector that completes the direct triad $(\boldsymbol{\Omega}_{\text{MAG}}, \mathbf{B}, (\mathbf{v} \cdot \nabla) \mathbf{B})$ (ensuring the homogeneity of the formula), hence,

$$\boldsymbol{\Omega}_{\text{MAG}} = \mathbf{b} \times ((\mathbf{v} \cdot \nabla) \mathbf{b}) \quad (25)$$

Thus, without neglecting the ‘‘convective term’’, and assuming that \mathbf{B} is constant in norm along the trajectory and is constant w.r.t. time at an inertially fixed point in space, we derive the following expression of the control torque in the case of the bDot controller

$$\begin{aligned} \mathbf{m} &= -\frac{k}{\|\mathbf{B}\|} \left(\left. \frac{d\mathbf{b}}{dt} \right|_{\mathcal{I}} - \boldsymbol{\omega} \times \mathbf{b} \right) \\ &= -\frac{k}{\|\mathbf{B}\|} ((\mathbf{v} \cdot \nabla)\mathbf{b} - \boldsymbol{\omega} \times \mathbf{b}) \\ &= -\frac{k}{\|\mathbf{B}\|} ((\boldsymbol{\Omega}_{\text{MAG}} - \boldsymbol{\omega}) \times \mathbf{b}) \end{aligned} \quad (26)$$

$$\begin{aligned} \mathbf{L}_{\text{MAG}} &= -k [\mathbf{I}_3 - \mathbf{b}\mathbf{b}^T] \tilde{\boldsymbol{\omega}} \\ \text{with, } \tilde{\boldsymbol{\omega}} &= (\boldsymbol{\omega} - \boldsymbol{\Omega}_{\text{MAG}}) \end{aligned} \quad (27)$$

we found the exact expression of the biased bDot control law (Eq. (17)). This amounts to $\boldsymbol{\omega}$ having the magnetic field rotation vector as an added setpoint. Because of the magnetic field’s shape, for polar orbits, we should expect $\boldsymbol{\Omega}_{\text{MAG}}$ to have a magnitude of about twice the orbital natural frequency ω_0 and to be in the orbit normal direction. Reference [5] shows that its magnitude is in fact $1.8\omega_0$.

In the case of a biased bDot controller, the setpoint simply becomes $\boldsymbol{\Omega}_{\text{bias}} + \boldsymbol{\Omega}_{\text{MAG}}$.

Since both controllers amount to a biased bDot control law, let us study the stability of it.

5. Stability analysis of the biased bDot control law

Let us look at this new Lyapunov candidate function :

$$V(\tilde{\boldsymbol{\omega}}) = \frac{1}{2} \tilde{\boldsymbol{\omega}}^T \mathbf{I} \tilde{\boldsymbol{\omega}} \quad (28)$$

$$\begin{aligned} \dot{V}(\tilde{\boldsymbol{\omega}}) &= \tilde{\boldsymbol{\omega}}^T \mathbf{I} \dot{\tilde{\boldsymbol{\omega}}} \\ &= \tilde{\boldsymbol{\omega}}^T \mathbf{I} (\dot{\boldsymbol{\omega}} - \dot{\boldsymbol{\Omega}}) \\ &= -k \tilde{\boldsymbol{\omega}}^T [\mathbf{I}_3 - \mathbf{b}\mathbf{b}^T] \tilde{\boldsymbol{\omega}} - \tilde{\boldsymbol{\omega}}^T \mathbf{I} \dot{\boldsymbol{\Omega}} \end{aligned} \quad (29)$$

Provided the setpoint time derivative is zero or negligible in the body frame, we have :

$$\dot{V}(\tilde{\boldsymbol{\omega}}) = -k \tilde{\boldsymbol{\omega}}^T [\mathbf{I}_3 - \mathbf{b}\mathbf{b}^T] \tilde{\boldsymbol{\omega}} \quad (30)$$

which is similar to Eq. (20).

Again, using LaSalle’s invariance principle

$$S = \{\mathbf{b}\mathbf{b}^T = \mathbf{I}_3 \text{ or, } \tilde{\boldsymbol{\omega}} // \mathbf{b}\}$$

Since $\mathbf{b}\mathbf{b}^T$ is a rank 1 matrix and \mathbf{I}_3 a rank 3 matrix, $\mathbf{b}\mathbf{b}^T \neq \mathbf{I}_3, \forall \mathbf{b}$. Thus,

$$S' = \{\tilde{\boldsymbol{\omega}} // \mathbf{b}\}$$

There are several cases here :

- If $\tilde{\boldsymbol{\omega}} = \mathbf{0}$, regardless of the expression of \mathbf{b} at the next instant, we will always have $\tilde{\boldsymbol{\omega}} \in S'$. This is therefore a truly stable case.

- If $\tilde{\boldsymbol{\omega}} = \boldsymbol{\omega} - \boldsymbol{\Omega} \neq \mathbf{0}$ and collinear with \mathbf{b} :
 - If $\boldsymbol{\omega}$ is not collinear with \mathbf{b} , the expression of the latter changes, which implies that $\tilde{\boldsymbol{\omega}} \in S'$ ($\tilde{\boldsymbol{\omega}}$ is no longer collinear with \mathbf{b}). This is therefore not a stable case.
 - If $\boldsymbol{\omega}$ is collinear with \mathbf{b} (so $\boldsymbol{\Omega}$ is also):
 - * If \mathbf{b} is inertial, then its expression does not change, so $\tilde{\boldsymbol{\omega}}$ is always collinear with \mathbf{b} . This is therefore a stable case.
 - * If \mathbf{b} varies over time in an inertial frame, its expression also changes in the satellite frame, and therefore $\tilde{\boldsymbol{\omega}}$ will no longer be collinear with \mathbf{b} at the next instant. This is therefore not a stable case.

In conclusion,

$$S' = \left\{ \begin{array}{l} \tilde{\boldsymbol{\omega}} = \mathbf{0}; \\ \boldsymbol{\omega} \text{ and } \boldsymbol{\Omega} \text{ collinear with } \mathbf{b} \text{ and } \mathbf{b} \text{ inertial} \end{array} \right\} \quad (31)$$

Therefore, using a bDot or biased bDot controller in polar orbits, we should expect the satellite to converge respectively to $\boldsymbol{\Omega}_{\text{MAG}}$ or $\boldsymbol{\Omega}_{\text{MAG}} + \boldsymbol{\Omega}_{\text{bias}}$, since \mathbf{b} changes a lot during one orbit in this case. In equatorial orbits, since \mathbf{b} is almost inertial, we might converge to the second equilibrium case, where $\boldsymbol{\omega}$ becomes colinear to \mathbf{b} .

E. Simulation settings

As explained above, the aim of the simulations is to explore the effect of the inclination on the satellite behavior. In order to have results which can be generalized and that are likely not due to coincidence, additional parameters are swept (such as orbital parameters, initial attitude, etc.). All of these parameters are detailed in the following sections (II.E.1, II.E.2, II.E.3).

1. Fixed simulation settings

The following parameters remain constant across all simulations.

- **Orbital parameters:** They are being given in Keplerian coordinates, which was motivated by [6]. Inclination and RAAN are swept parameters, so they are defined in the next paragraph.
 - **Semi-major axis:** $a \approx 7000$ km
 - * Meaning the orbital period is: $T_{\text{orbit}} \approx 6000$ s $\approx 1\text{h}40\text{min}$
 - * And the mean altitude is: $h \approx 600$ km
 - **Eccentricity:** $e \ll 1$, quasi-circular orbit
 - **Initial mean anomaly:** $M = 0^\circ$
- All disturbances are taken into account: magnetic torque, gravity gradient, aerodynamic pressure, solar radiation, sensor biases and noise.
 - For solar radiation and aerodynamic pressures, the coefficients depending on angle of attack

and satellite geometry were determined using an external software, this method is not detailed here.

- **Simulation time:** $T = 2$ days. Preliminary result showed that in some cases, for near equatorial orbits, the detumbling can take as long as 1.5 days. Two days was chosen to have some margin on that duration.
- **Starting date:** It was decided that the simulation would start January 1st 2027 at 00:00:00.
- **Mass :** $m = 5.5$ kg
- **Control law:** the satellite attitude is controlled using the biased bDot law. Here, the satellite is spun around its axis of minimal inertia (Z axis). Based on (13), the magnetic moment control law is the following:

$$\mathbf{m}_{\text{bias}} = \mathbf{b} \times \left(\frac{-\mathbf{K}}{\|\mathbf{B}\|} (\dot{\mathbf{b}} + \boldsymbol{\Omega}_{\text{bias}} \times \mathbf{b}) \times \mathbf{b} \right) \quad (32)$$

The design of the control gain matrix \mathbf{K} is not detailed in this study.

- **Solar activity:** this not only induces solar radiation pressure but also influences atmospheric density, which is significant in LEO. Indeed, high solar activity heats the atmosphere up and increases its density, causing more atmospheric drag.
 - F10.7 solar flux = 140 sfu
 - Geomagnetic index : AP = 15

2. Swept parameters

Every combination of parameters listed here results in one simulation configuration. The set of all simulation configurations is then the Cartesian product of the parameter sets.

- **Angular velocity:**
 $\boldsymbol{\omega}_{\text{init}} = 10^\circ/\text{s} \times (\text{XSat}, \text{YSat}, \text{ or } \pm \text{ZSat})$. The value of $10^\circ/\text{s}$ was estimated to be the upper bound of what a typical Cubesat might experience after separation from the second stage of a rideshare launch.
- **Initial attitude quaternion:** q_{Sat} is chosen such that either $\pm \text{ZSat}$ or XSat is initially colinear to the magnetic field direction. The $\pm \text{ZSat}$ case was expected to be the configuration where it is the hardest to reach the setpoint as initially no control torque can be exerted on the spinning axis ZSat.
- **Residual magnetic moment:**
 $\mathbf{m}_{\text{Res}} = (0, 10 \text{ or } 20 \text{ mAm}^2) \times (\text{XSat}, \text{YSat or ZSat})$. This parameter was expected to have a significant impact on results as it creates a bias on the actuation torque.
- **Orbit inclination:** 15 equally spaced angles from 0° to 97.71° , the latter value corresponding to the inclination of a sun-synchronous orbit at the chosen semi-major axis.
- **RAAN:** 8 values equally spaced ranging from 0 to π . The starting date was fixed, so having variation on

RAAN allowed to obtain different initial alignments with the Earth's magnetic field.

This leads to a total number of simulations:

$$N = 4 \times 3 \times 7 \times 15 \times 8 = 10\,080$$

3. Randomized parameters

In order to obtain more variability between each simulations, random noise is added to some parameters each time a simulation starts, including: inertia matrix, sensors bias and misalignment, and coupling between magnetorquers and magnetometers.

F. Derivation of results

This section details the methodology employed to derive the key results presented in this study.

1. Convergence time

The goal of ASM mode is mainly to detumble the satellite and point its solar arrays towards the Sun. Depending on mission design, these two objectives can be targeted simultaneously or in two separate phases. When implemented separately, detumbling is done first before Sun pointing starts. This means that detumbling must be achieved before the satellite batteries reach a critical threshold beyond which there is not enough power left to run the Sun pointing phase. This power requirement typically determines battery sizing. For this study, which focuses exclusively on detumbling performance, the success criterion is achieving convergence within two orbits.

Convergence time was defined as explained below. A more detailed justification of this criteria can be found in the appendix V.0.a.

$$t_{\text{conv}} \text{ s.t. } \begin{cases} \|\boldsymbol{\varepsilon}(t) - \bar{\boldsymbol{\varepsilon}}\| \leq 0.2^\circ/\text{s}, \\ \text{for at least 90\% of } t \geq t_{\text{conv}} \\ \left| \frac{d\|\boldsymbol{\varepsilon}(t)\|}{dt} \right| \leq 0.1^\circ/\text{s}^2, \\ \forall t \geq t_{\text{conv}} \end{cases} \quad (33)$$

with,

- $\boldsymbol{\varepsilon}(t) = \boldsymbol{\omega}(t) - \boldsymbol{\Omega}$
- $\boldsymbol{\Omega}$ angular velocity setpoint,
- $\bar{\boldsymbol{\varepsilon}}$ mean value during last whole orbit of simulation.

In other words, after the convergence time, at least 90% of the error is at most $0.2^\circ/\text{s}$ away from its mean value during last orbit, and the slope of the error is lower than $0.1^\circ/\text{s}^2$.

The value of $0.2^\circ/\text{s}$ was chosen as it is approximately 10% of the angular velocity setpoint magnitude.

2. Pointing error between two vectors

The pointing error was computed as such

$$\delta(\mathbf{u}, \mathbf{v}) = \widehat{\mathbf{u}, \mathbf{v}} \quad (34)$$

with, $\widehat{\mathbf{u}, \mathbf{v}}$ the geometric angle between \mathbf{u} and \mathbf{v} .

3. Convergence time of pointing error

The convergence time of pointing error is computed as such

$$t_{\text{conv},\delta} \text{ s.t. } \delta(\mathbf{u}, \mathbf{v})(t) \leq 45^\circ, \forall t \geq t_{\text{conv},\delta} \quad (35)$$

In other words, after the pointing error convergence time, the two vectors are never more than 45° apart.

4. Convergence diagram

In the convergence diagram (III.A.7), the envelope of $\|\varepsilon(t)\|$ for each simulation is plotted. The envelope is defined as such

$$M(x)(t) = \max(x(\tau), \forall \tau \geq t) \quad (36)$$

In other words, the envelope of a value at time t is the maximum of that value after t .

III. RESULTS

A. Simulation parameter sweep

1. Convergence time

Figure 3 shows the graph of the convergence time of each simulation sorted by orbit inclination

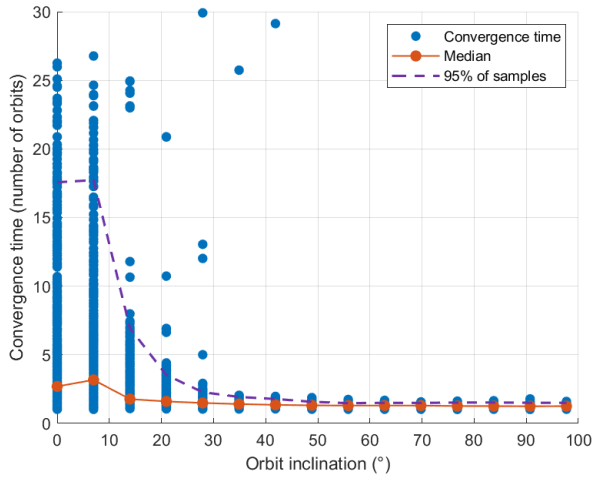


Fig. 3: Convergence time per orbit inclination

A trend could be noticed: the convergence time and its deviation decreased as orbit inclination increased, going from a median time of 3.17 to 1.26 orbits.

Median time is below the convergence criterion of 2 orbits (see II.F.1) starting from an inclination of 13.95° .

95th percentile time is below the convergence criterion of 2 orbits starting from an inclination of 34.90° .

The results are discussed in (IV.A.1).

2. Mean angular velocity error to setpoint

Figure 4 represents the mean angular velocity error to setpoint (i.e. static error) during last orbit w.r.t. orbit inclination:

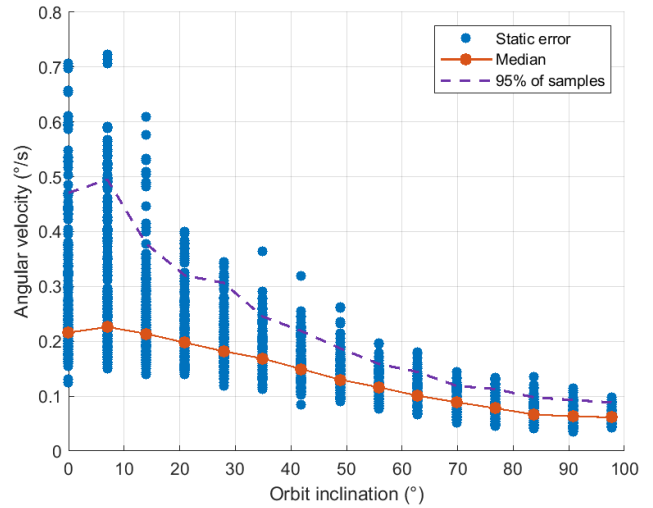


Fig. 4: Mean angular velocity error to setpoint during last orbit as a function of orbit inclination

Overall, it could be observed that the static error median and 95th percentile decreased as inclination increased. Their highest values are respectively $0.23^\circ/\text{s}$ and $0.49^\circ/\text{s}$, both are reached at an inclination of 6.98° .

The results are discussed in IV.A.2.

3. Peak to peak of angular velocity error to setpoint

Figure 5 shows the Peak To Peak (P2P) value of angular velocity error to setpoint during the last orbit as a function of orbit inclination:

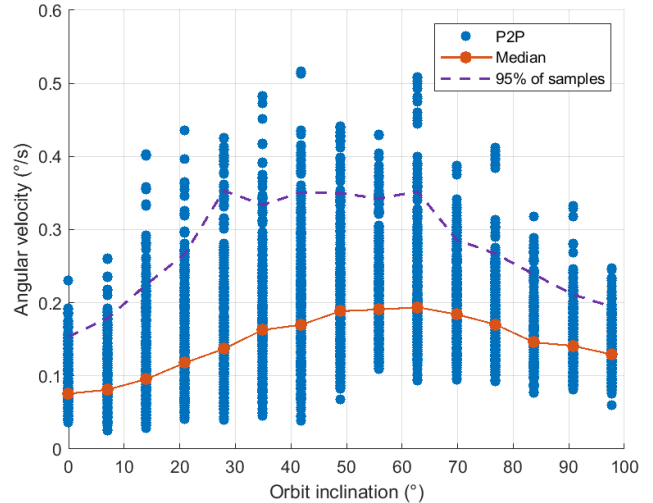


Fig. 5: Peak to peak of angular velocity error to setpoint during the last orbit as a function of orbit inclination

The analysis reveals that the P2P median angular velocity began at $0.08^\circ/\text{s}$ (0° inclination) and increased to a maximum of $0.19^\circ/\text{s}$ at 62.81° inclination before decreasing to a final value of $0.13^\circ/\text{s}$. Similarly, the 95th percentile started at $0.15^\circ/\text{s}$ (0° inclination), rose to $0.35^\circ/\text{s}$ by 27.91° , maintained this value through 62.81° , and then declined to $0.19^\circ/\text{s}$ for higher inclinations.

This is discussed in IV.A.3.

4. Mean pointing error of ZSat axis w.r.t. orbit normal

Figure 6 represents the mean pointing error between the satellite ZSat axis and the orbit normal during last orbit as a function of orbit inclination:

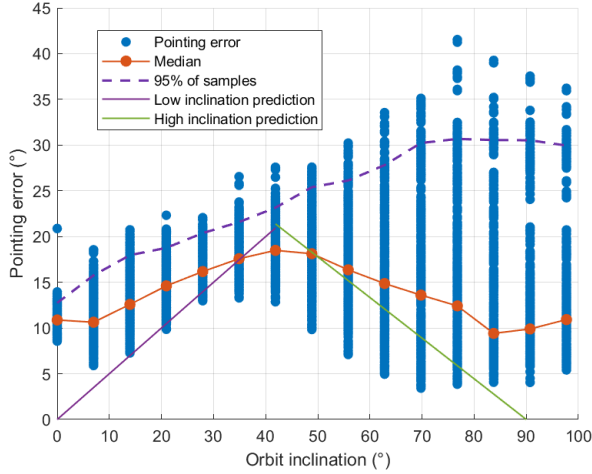


Fig. 6: Pointing error of ZSat axis w.r.t. orbit normal during last orbit per orbit inclination

According to [5], the spin axis is predicted to deviate roughly $\frac{1}{2}i$ from the orbit normal in near-equatorial orbits and $\frac{4}{9}(\pi/2 - i)$ in polar orbits, where i represents the orbit inclination. These predictions are also illustrated in the graph.

It could be noticed that the variability increased as inclination increased, while median increased and reached a peak of 41.51° at 76.77° of inclination before decreasing. The results are discussed in (IV.A.4).

5. Convergence time of pointing error of ZSat axis w.r.t. orbit normal

Figure 7 shows the convergence time of pointing error between the satellite ZSat axis and the orbit normal as a function of orbit inclination.

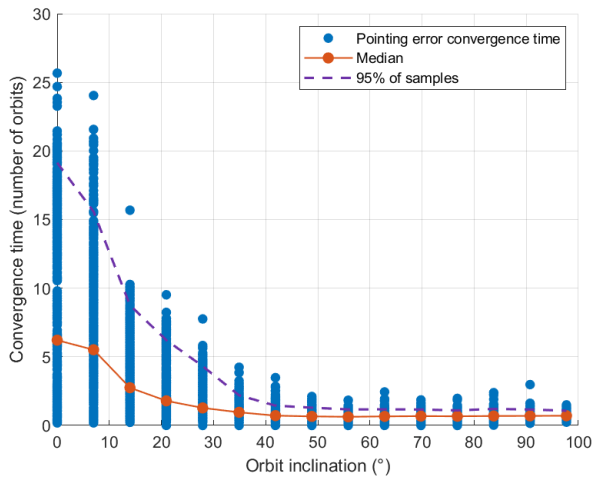


Fig. 7: Convergence time of pointing error of ZSat axis w.r.t. orbit normal per orbit inclination

A trend could be noticed, where convergence time median and 95th percentile decrease as orbit inclination increases. The maximum convergence time, of 25.67 orbits, was reached at an equatorial orbit.

Median time is below the convergence criterion of 2 orbits (see II.F.1) starting from an inclination of 20.94° .

95th percentile time is below the convergence criterion of 2 orbits starting from an inclination of 41.88° .

The results are discussed in (IV.A.5).

6. Actuator saturation

Figure 8 represents a graph of percentage of time at which the MTQs are saturated per orbit inclination:

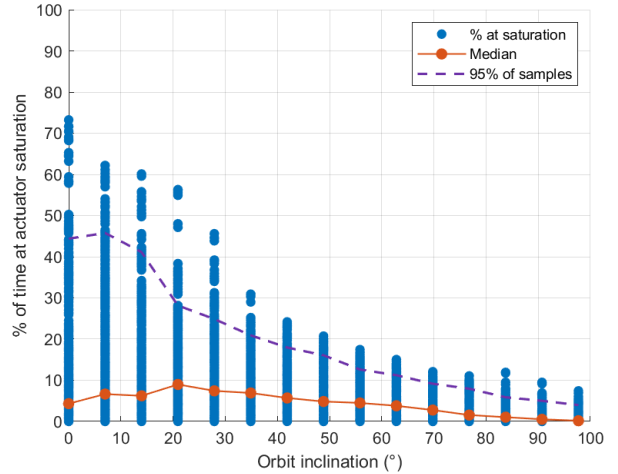


Fig. 8: MTQ saturation percentage of time per orbit inclination

An overall decrease of actuator saturation was observed as orbit went from equatorial to polar. The median increased to a maximum of 8.91% at 20.94° and then decreased. 95th percentile dropped as inclination decreased.

The results are discussed in (IV.A.6).

7. Convergence diagram

Figure 9 shows the graph of the envelope of $\|\varepsilon(t)\|$ for every simulation. It is colored per orbit inclination.

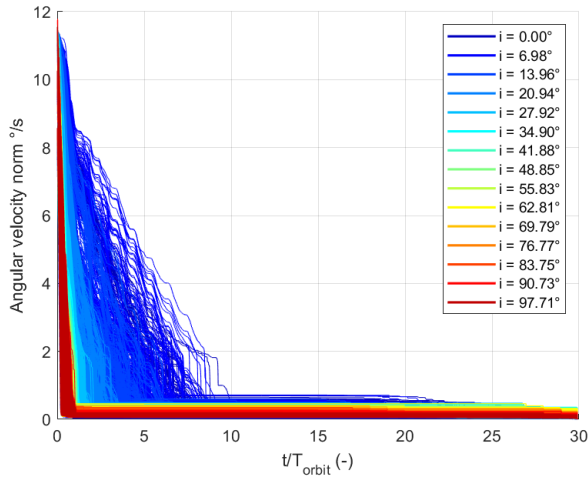


Fig. 9: Simulation convergence diagram colored by orbit inclination

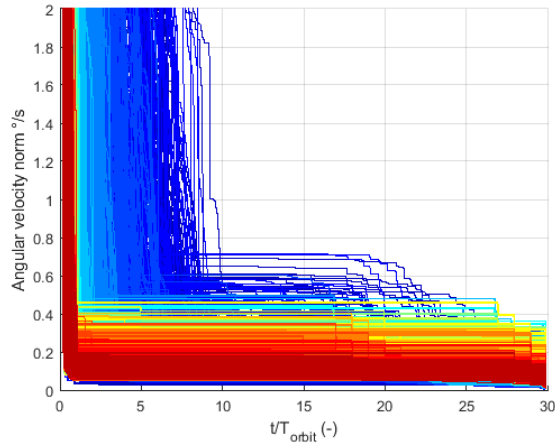


Fig. 10: Simulation convergence diagram colored by orbit inclination zoomed around the $[0, 2]^\circ/\text{s}$ y-axis area

It was observed that the convergence plots decrease was faster as the orbit inclination was larger. Some simulations at low inclination orbits had a constant value for more than 10 orbits before dropping to a lower value (see on Figure 10). This behavior was shown in more detail in (III.B.3).

The results are discussed in (IV.A.7).

8. Convergence time results grouped by other initial conditions

Figures 11 to 14 show the histograms representing the sensitivity of convergence time to the other significant initial conditions for simulations having a convergence time above the criterion of 2 orbits.

The results are discussed in (IV.A.8).

a. Grouped by initial angular velocity

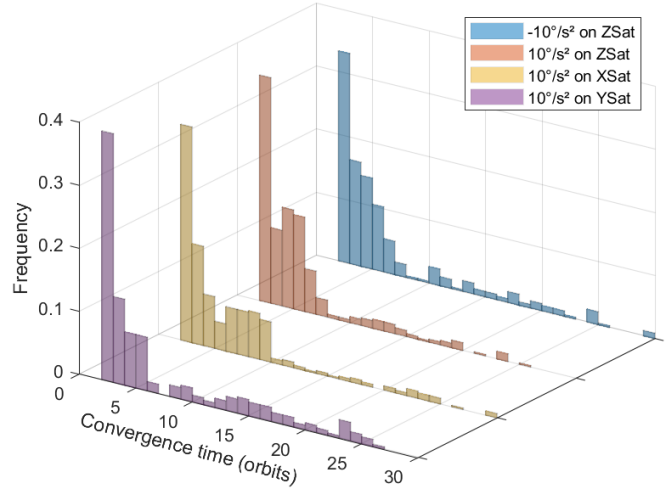


Fig. 11: Histograms of convergence time per initial angular velocity for simulations with $t_{\text{conv}} > 2$ orbits

The analysis revealed variations in the spread of values. Initial angular velocity aligned with XSat produced the greatest spread, while alignment with the ZSat or $-Z\text{Sat}$ axes resulted in moderate spread. The smallest spread occurred when ω_{init} was aligned with the Y-axis.

b. Grouped by initial axis aligned with B

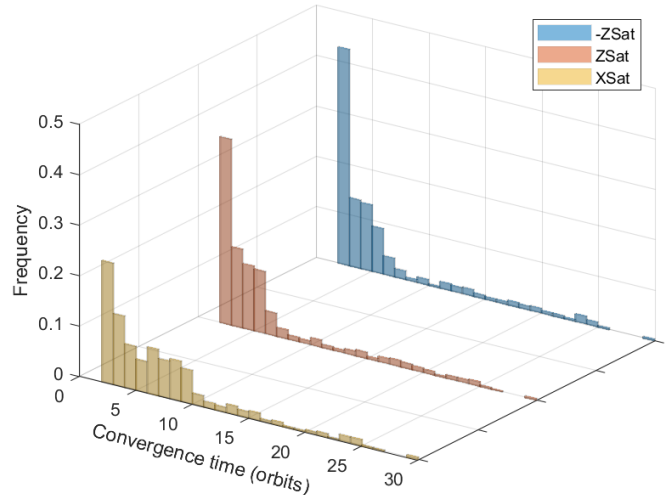


Fig. 12: Histograms of convergence time per axis aligned with B for simulations with $t_{\text{conv}} > 2$ orbits

It could be noticed that having XSat initially aligned with B yielded the most spread of values. ZSat or $-Z\text{Sat}$ aligned with B showed similar results with a smaller spread.

c. Grouped by residual magnetic moment

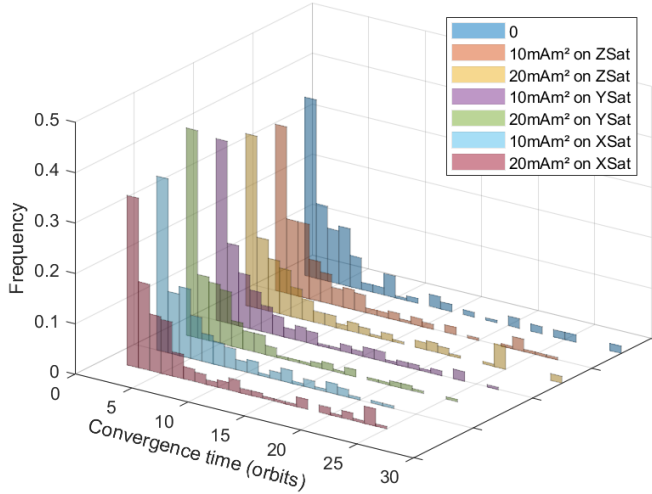


Fig. 13: Histograms of convergence time per residual magnetic moment for simulations with $t_{conv} > 2$ orbits

The spread of convergence time values was similar for all residual magnetic moment values.

d. Grouped by RAAN

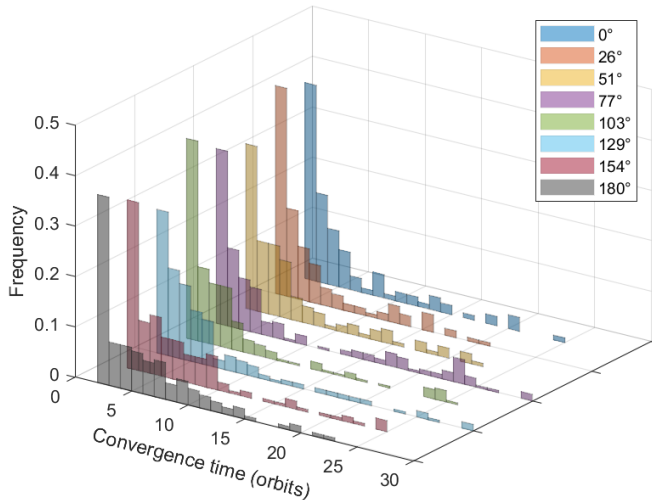


Fig. 14: Histograms of convergence time per RAAN for simulations with $t_{conv} > 2$ orbits

It could be observed that the convergence time values had similar results for RAANs between 0° and 129° while the spread was more consequent for RAANs of 154° and 180° .

9. Mean pointing error of ZSat axis w.r.t. orbit normal grouped by residual magnetic moment

Figures 15 and 16 show the sensitivity of mean pointing error of ZSat axis w.r.t. orbit normal based on the axis where residual magnetic moment was present.

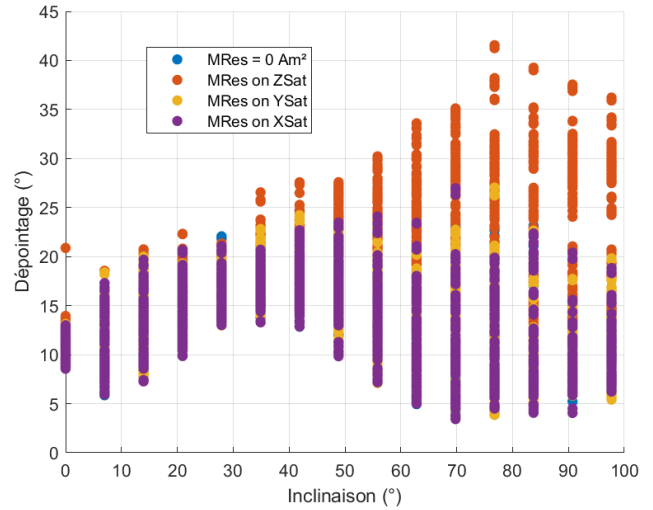


Fig. 15: Mean pointing error of ZSat axis w.r.t. orbit normal. Points are colored based on the axis where residual magnetic moment was present

It could be noticed that having residual magnetic moment on ZSat increased pointing error between ZSat and orbit normal for inclinations above 40° significantly compared to the other axes. Having residual magnetic moment on either XSat or YSat or no residual magnetic moment at all yielded similar results.

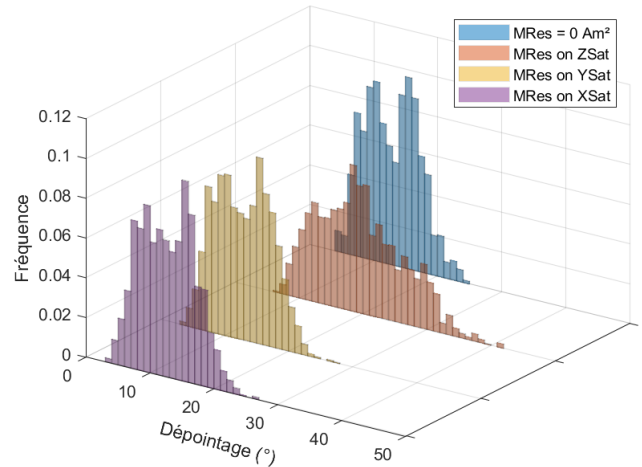


Fig. 16: Histograms of mean pointing error of ZSat axis w.r.t. orbit normal per axis where residual magnetic moment was present

It could be observed that the histogram where residual magnetic moment is on ZSat is much more spread out than the others. Having residual magnetic moment on either XSat or YSat or no residual magnetic moment at all yielded similar histograms.

The results are discussed in (IV.A.9).

B. Single simulation study

In this section, a few simulations are being studied in more detail, in order to get a better understanding of the problem.

1. Traces of \mathbf{b} and ZSat axis

Figures 17 to 22 show the traces of \mathbf{b} and ZSat axis over a simulation of 2 days, for three different orbits: equatorial, 45° inclination and SSO. The trace of a unit vector is defined as the points on the unit circle left by that vector as its direction changes over time.

a. Direction of \mathbf{B} :

The results are discussed in Paragraph IV.B.1.a.

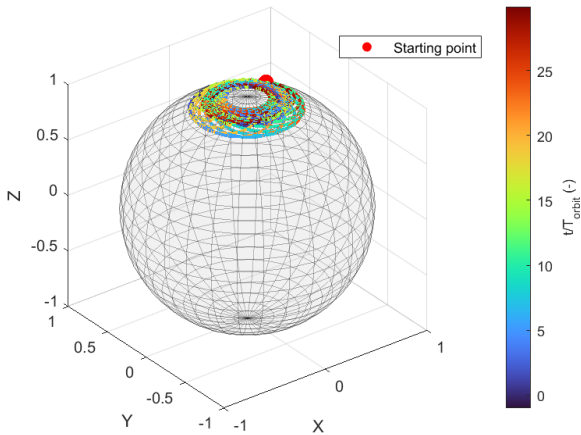


Fig. 17: Trace of the direction of magnetic field seen by the satellite along its trajectory for an equatorial orbit and for 2 days of simulation time

It could be observed that \mathbf{b} evolved in a constrained area around the inertial Z axis, which was also the orbit normal. The minimal and maximal deviations from the latter were respectively 27.1° and 9.7° .

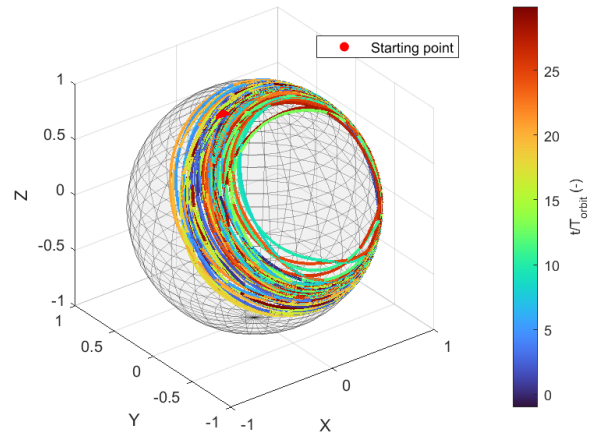


Fig. 18: Trace of the direction of magnetic field seen by the satellite along its trajectory for a 45° inclination orbit and for 2 days of simulation time

At 45° of inclination, it could be noticed that the trace left by \mathbf{b} was constrained to a conical shape the axis of which was close to the orbit normal. The mean axis of the cone had a deviation of 11.8° from the orbit normal. The minimal and maximal deviations from the cone axis are respectively 36.7° and 74.3° .

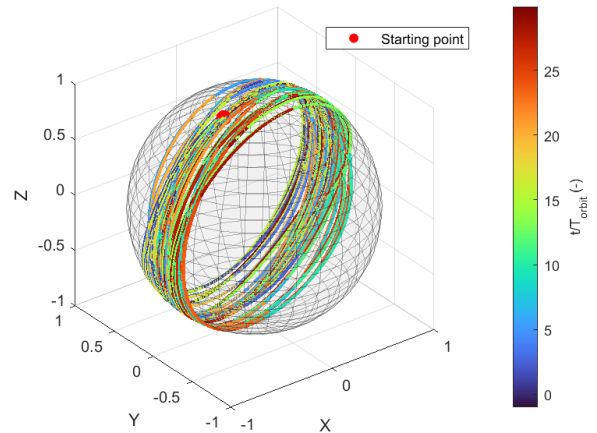


Fig. 19: Trace of the direction of magnetic field seen by the satellite along its trajectory for an SSO and for 2 days of simulation time

In an SSO, it could be observed that the trace of \mathbf{b} was describing circles going from $+Z$ to $-Z$. All of the circles were approximately normal to the orbit normal.

b. Direction of ZSat axis :

The results are discussed in Paragraph IV.B.1.b.

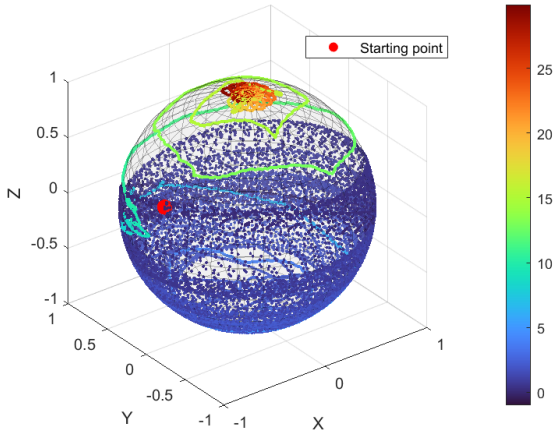


Fig. 20: Trace of ZSat axis along satellite trajectory for an equatorial orbit and for 2 days of simulation time

In an equatorial orbit, ZSat initially rotated covering a large part of the circle before converging to the vicinity of the inertial Z. Based on the color bar, it can be observed that ZSat got close to Z late in the simulation. The minimal and maximal deviations from the Z axis during the last five orbits are respectively 0.04° and 12.96° .

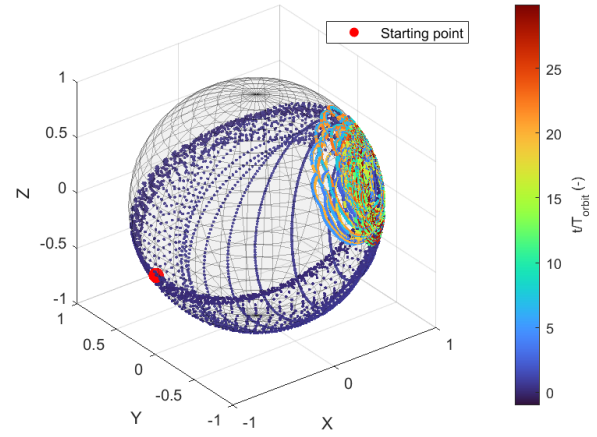


Fig. 22: Trace of ZSat axis along satellite trajectory for an SSO and for 2 days of simulation time

In an SSO, ZSat converged to a conical area the mean axis of which is 43.21° away from the orbit normal. The minimal and maximal deviations from the orbit normal during the last five orbits are respectively 11.47° and 77.51° .

2. External torques

Figure 23 shows a plot of the four disturbance torques norm during a 2 day long simulation of the system, for a typical sun-synchronous orbit, with a residual magnetic moment of 0.02 Am^2 on the Z axis:

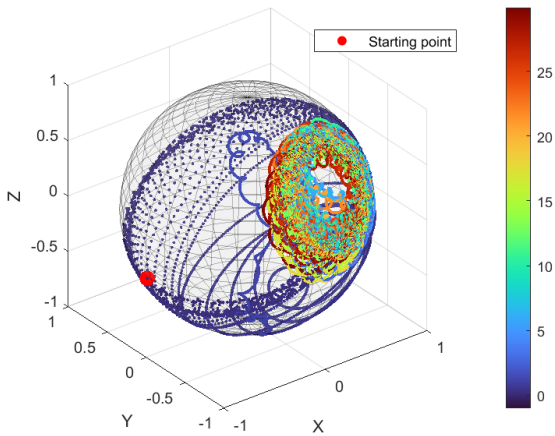


Fig. 21: Trace of ZSat axis along satellite trajectory for a 45° inclination orbit and for 2 days of simulation time

At a 45° inclination, ZSat converged to a conical area the mean axis of which is 6.63° away from the orbit normal. The minimal and maximal deviations from the orbit normal during the last five orbits are respectively 0.24° and 52.22° .

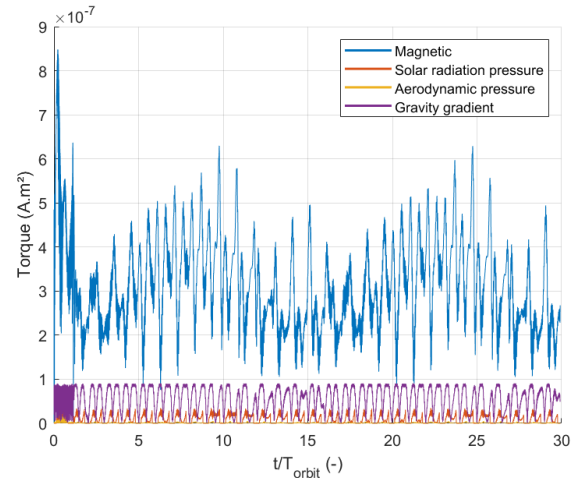


Fig. 23: Norm of the four disturbance torques for a sun-synchronous orbit, with a residual magnetic moment of 0.02 Am^2 on the Z axis and for 2 days of simulation time

In terms of magnitude, the largest disturbance torque was the magnetic torque, followed gravity gradient. Solar radiation and aerodynamic pressures were the smallest, both having the same order of magnitude.

The results are discussed in (IV.B.2).

3. Metastable state at low inclination orbits

During the analysis, three distinct simulation scenarios were examined through angular velocity error plots and MTQ command magnetic moment data:

- One simulation displayed metastable behavior
- Another represented typical performance in a SSO
- The third case illustrated behavior in an equatorial orbit without a metastable behavior

Figures 24 to 29 show these three behaviors. It should be noted that the MTQ maximum magnetic moment is 0.2 Am² on each axis.

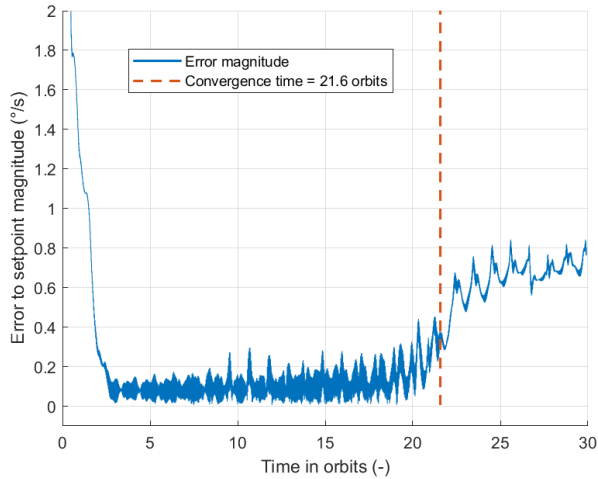


Fig. 24: Magnitude of error to angular velocity setpoint as a function of time for a simulation with a metastable behavior. Orbital parameters: $i = 6.98^\circ$, $\Omega = 77.14^\circ$

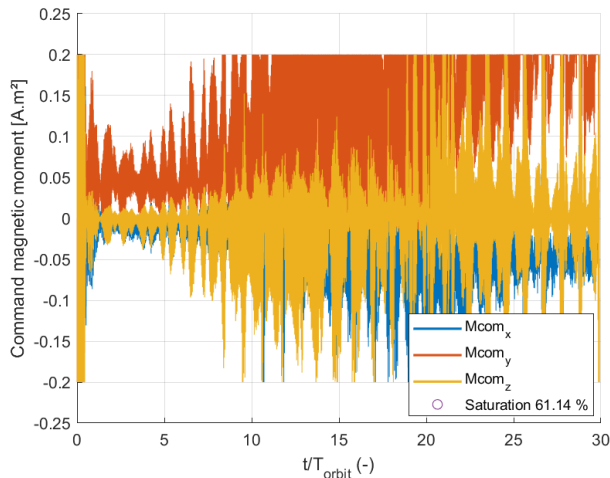


Fig. 25: MTQ magnetic moment as a function of time for a simulation with a metastable behavior. Orbital parameters: $i = 6.98^\circ$, $\Omega = 77.14^\circ$

It could be noticed a transient of approximately 2 orbits before a stabilization of the error magnitude for around 16 orbits. Then, a new transient appeared and a new stable state with higher error magnitude was

reached. The static error of the final stable state is $0.71^\circ/s$.

The analysis revealed that the MTQs initially operated well below its saturation limit following the first convergence. Over time, the three axes gradually approached saturation and maintained high-frequency oscillations between saturation and lower actuation levels. After reaching the second stable state, the y-axis exhibited less oscillation while remaining closer to saturation. Overall, the MTQ were saturated 61.14% of the time.

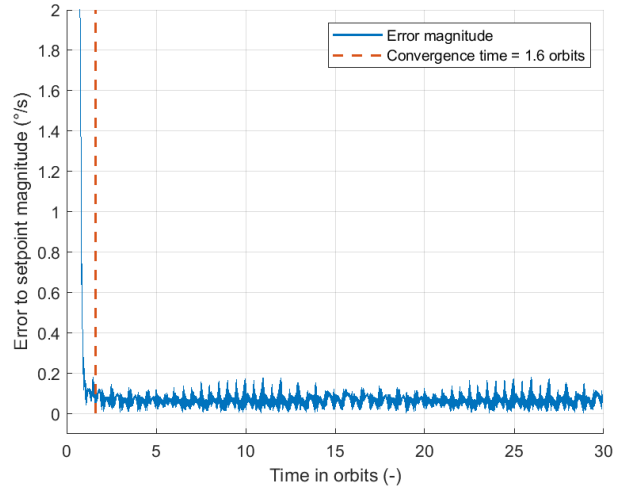


Fig. 26: Magnitude of error to angular velocity setpoint as a function of time for a fast convergence time simulation. Orbital parameters: $i = 97.71^\circ$, $\Omega = 0^\circ$

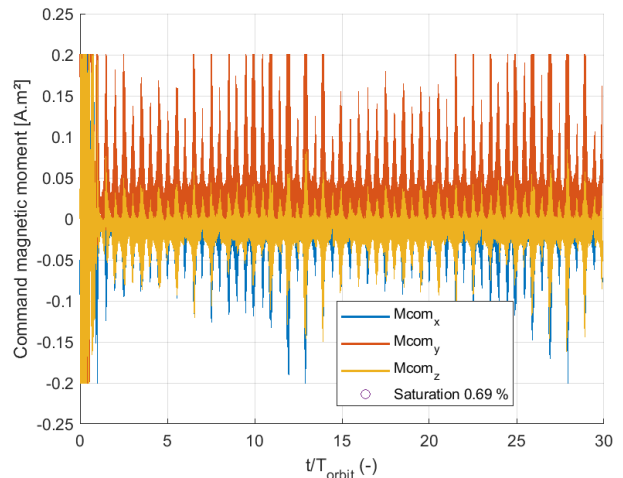


Fig. 27: MTQ magnetic moment as a function of time for a fast convergence time simulation. Orbital parameters: $i = 97.71^\circ$, $\Omega = 0^\circ$

The error converged to near zero value in 1.6 orbits and remained in an oscillatory state for the rest of the simulation. Its mean deviation from 0 is $0.069^\circ/s$.

The MTQs rarely reached saturation, maintaining operation well below this threshold throughout the simulation. Saturation occurred for only 0.69% of the total time.

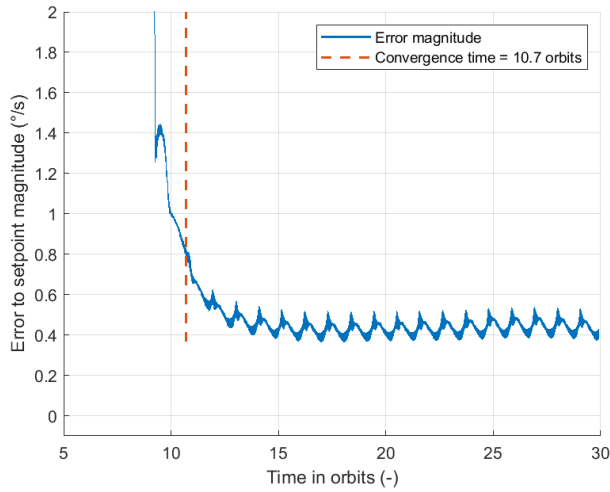


Fig. 28: Magnitude of error to angular velocity setpoint as a function of time for a typical slow convergence time simulation. Orbital parameters: $i = 0^\circ$, $\Omega = 0^\circ$

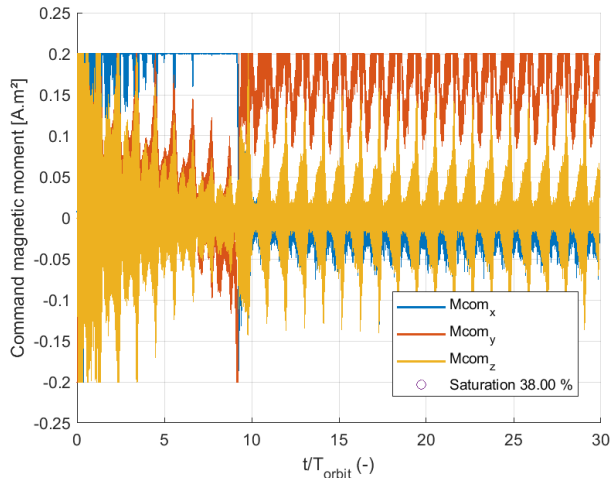


Fig. 29: MTQ magnetic moment as a function of time for a typical slow convergence time simulation. Orbital parameters: $i = 0^\circ$, $\Omega = 0^\circ$

The error converged to an oscillatory state in 10.7 orbits and its mean deviation from zero is $0.44^\circ/\text{s}$.

During transient, the x-axis remained mostly saturated while y- and z-axes progressively decreased in saturation. In the stable state, x- and z-axes functioned below saturation thresholds with oscillations between high and low actuation, whereas the y-axis continued oscillating between high actuation and saturation. The MTQs were saturated 38.00% of the time.

The results are discussed in (IV.B.3).

IV. DISCUSSION

A. Simulation parameter sweep

1. Convergence time

Figure 3 demonstrates that the biased bDot control successfully detumbles the satellite within two orbits in:

- 95% of cases for inclinations above 34.90°
- 50% of cases for inclinations greater than 13.95°

At lower inclinations, too long of a convergence time would mean that the satellite batteries have discharged before it could reach the setpoint. This was coherent with theory, since \mathbf{B} became increasingly more inertial as orbit inclination decreased, control authority around the direction of it became weaker.

It can be noticed that the 6.98° inclination orbit yielded higher convergence time results than equatorial orbits. This could be explained by the fact that control authority was the weakest when the direction of \mathbf{B} varied the least. This happened when the orbit normal was the closest to the geomagnetic poles axis, which has an estimated declination of 4.2° in 2027. Thus, the closest inclination to this in the simulation was the 6.98° one.

Furthermore, while the median convergence time remained low even at low inclination orbits, the 95th percentile convergence time increased significantly as the orbit inclination approached zero. This indicates a growing spread in convergence times, with a notable increase in the upper tail of the distribution as inclination decreased. This behavior was hard to explain simply with the individual simulation initial conditions, as even close initial conditions may have very different convergence times. It could then be inferred that the system may become chaotic for low inclination orbits, starting from 41.88° .

2. Mean angular velocity error to setpoint

Figure 4 demonstrates that control performance in terms of static error improves with increasing orbit inclination. This trend can be attributed to the fact that the magnetic field vector \mathbf{b} is almost inertial at low inclinations. Additionally, Figure 6 reveals that the spin axis aligns closely with \mathbf{b} at these inclinations. Thus, any angular velocity error in the direction of \mathbf{b} cannot be corrected by the controller, as this direction is uncontrollable.

3. Peak to peak of angular velocity error to setpoint

Figure 5 reveals a peak in P2P error at mid-inclination orbits, indicating that the oscillation amplitude in the converged state (as shown in Figures 24, 26 and 28) is particularly high for these inclinations. Additionally, results exhibit greater variability at these amplitudes, which is counterintuitive as one would expect poorer control performance at lower inclinations. This unexpected behavior remains unexplained.

This observation provides insight into why some simulations showed high convergence times around $20\text{--}40^\circ$ inclination, Figure 3. The substantial oscillations in the converged state for these cases exceeded the 90% of error below $0.2^\circ/\text{s}$ convergence criterion (Section II.F.1), thus contributing to the extended convergence times.

4. Mean pointing error of ZSat axis w.r.t. orbit normal

Figure 6 corroborates the findings of [5] and [7], demonstrating that both biased bDot and bDot control

laws result in a final attitude where the axis of maximum inertia (for bDot) or the spin axis (for biased bDot) aligns closely with the orbit normal. One hypothesis to explain this behavior is that the satellite axis actually aligns with the average axis of least controllability. The latter could be the trace of \mathbf{b} cone axis (see Paragraph III.B.1.a) since this is the closest direction to all directions of \mathbf{b} . Finally, since this axis is always very close to the orbit normal, this could explain why the satellite axis aligns with it.

Additionally, the pointing error generally follows the predicted trend lines. However, notable differences and variability exist around these trends, particularly the fact that the pointing error does not approach zero at either 0° or 90° inclination.

In addition, it is interesting to notice that pointing error variability is the highest for high inclination orbits, which is surprising as one could expect to have the most predictable behavior at these inclinations. III.A.9 reveals that this is actually due to residual magnetic moment (discussed in IV.A.9).

5. Convergence time of pointing error of ZSat axis w.r.t. orbit normal

Figure 6 shows that the satellite's attitude converges within the criterion of two orbits:

- 95% of cases for inclinations above 41.88°
- 50% of cases for inclinations greater than 20.94°

Moreover, similar results as in III.A.1 were obtained. The attitude and angular velocity convergence times were of the same order of magnitude. However, the worst case in terms of convergence time was reached at an equatorial orbit, instead of a 6.98° inclination.

This result was insightful to compare with angular velocity convergence since here, attitude convergence is measured.

6. Actuator saturation

The results in Figure 8 were coherent with what was observed regarding convergence time.

At low inclination, control authority diminished, which forced the MTQs to augment their magnetic moment to saturation frequently.

At high inclination, the little amount of saturation observed was due to the transient phase of convergence, when the error to setpoint was still large. Passed this, no saturation was observed since control authority was significant.

7. Convergence diagram

Based on Figure 9, the same conclusions as in Section IV.A.1 could clearly be drawn: convergence time decreased when orbit inclination increased. Variability of results at each inclination was hard to deduce from this figure. However, it gave some insight on the dynamics of the convergence. First, every simulation converged to equilibrium, there was not one reaching an unstable state. Plus, some simulations at low inclinations seemed

to reach a plateau at most around 10 orbits, although it could be seen in Figure 3 that simulations at such inclinations could reach a convergence time of more than 20 orbits. Thus, these simulations probably reach a metastable state before converging to their equilibrium. This was investigated in Section III.B.3.

8. Convergence time grouped by other initial conditions

Based on the results from Section III.A.8, it can be inferred that the values of high convergence time that are seen in all figures are due to the cases of high convergence times in low-inclination orbits.

In addition, linking the results of Figures 11 and 12, it can be concluded that the spread of results with XSat is likely due to the cases where the satellite starts with its initial angular velocity aligned with \mathbf{B} , which corresponds to low initial control authority.

Moreover, the same can be inferred from the cases where $\pm Z_{\text{Sat}}$ and $\pm \omega_{\text{init}}$ are aligned with \mathbf{B} as their histograms have very similar shapes. The spread is less important as inertia on ZSat is lower than on XSat meaning that the MTQs have a larger control authority in this case.

When looking at Figure 14, the fact that all histograms with $0^\circ \leq \Omega < 129^\circ$ is coherent as the orbit RAAN should not have any significant impact because of Earth's magnetic field near axisymmetry. However, no explanations for the differences in histogram shape for the $154^\circ \leq \Omega < 180^\circ$ cases were found.

Finally, based on Figure 13, it can be inferred that residual magnetic moment does not have any impact on the satellite's detumbling time. This is to some extent surprising since it was causing the largest disturbance torque (see Section IV.B.2). This lack of significant results may also be attributed to an insufficient quantization of directions and magnitude of this parameter relative to the frequency at which it influences the system.

Overall, compared to the effect of inclination on convergence time, these parameters have a minor impact on it.

9. Mean pointing error of ZSat axis w.r.t. orbit normal grouped by residual magnetic moment

Based on the results from Section III.A.9, a clear trend appears where residual magnetic moment on ZSat increases pointing error between ZSat and orbit normal for inclinations greater than 40° . This makes sense as residual magnetic moment on ZSat creates torque in the (XSat, YSat) plane, which rotates the ZSat axis.

Moreover, no significant effect was observed at low inclinations. This behavior can be attributed to the insufficient rotation of the magnetic field vector \mathbf{b} at these inclinations, which applies constraints on the satellite's final attitude.

B. Single simulation study

1. Traces of B and ZSat axis

a. Direction of B :

These results (Paragraph III.B.1.a) suggest that the magnetic field direction traces a path along the base of a conical surface. The axis of this cone consistently aligns closely with the orbit normal. As the orbit inclination increases, the cone's radius expands, ultimately transforming into a circular path when the cone's height diminishes to zero at polar orbit.

This aligns with the convergence time results: control authority improves with increasing orbit inclination, as the magnetic field direction sweeps through more spatial directions.

b. Direction of ZSat axis :

Based on the results (Paragraph III.B.1.b), it can be observed that the ZSat axis always converges to the vicinity of the orbit normal. This corroborates the results of Figure 6 and means that the spin axis always converges to being close to an inertial direction.

2. External torques

From Figure 23, it could be concluded that the largest torque exerted on the satellite was the magnetic torque, provided the spacecraft had a residual magnetic moment of 0.02 or 0.01 Am². In the case of no residual magnetic moment, the largest disturbance torque was the gravity gradient torque.

3. Metastable state at low inclination orbits

The presence of a metastable behavior in Figure 24 could be explained by considering the stability analysis done in Section II.D.5. There are two equilibria possible if \mathbf{b} is inertial, which was almost the case in this simulation, since the inclination was low (6.98°). The two equilibrium are either $\boldsymbol{\omega} = \mathbf{0}$, or $\boldsymbol{\omega}$ and $\boldsymbol{\Omega}$ colinear to \mathbf{b} . The second case could be possible here as, based on Figure 6, it is known that the ZSat axis always converged to being close to the orbit normal, the latter also being in the vicinity of B . This means that the axis of spin was almost colinear to B at some point in this case.

Thus, an explanation might be that the satellite first stabilized to the $\boldsymbol{\omega} = \mathbf{0}$ equilibrium, but, when ZSat became close enough to B , the state shifted to the $\boldsymbol{\omega}$ and $\boldsymbol{\Omega}$ colinear to \mathbf{b} equilibrium. Having the angular velocity close to the magnetic field direction would also explain why the error increased after reaching the second equilibrium, since control authority over it would diminish.

Compared with the other two cases, Figures 26 and 28, significant deviations from expected behavior were present. Indeed, typical simulations would show error converging to stable and low amplitude oscillations with slower convergence at low inclinations. Examination of MTQ actuation, Figures 25, 27 and 29, clearly illustrated reduced control authority in low inclination orbits,

as actuator saturation is much more frequent compared to SSO conditions.

All error plots, Figures 24, 26 and 28, had noticeable noise and periodic oscillations in the converged state. This observation highlights that while bDot control offers robustness and simplicity, it shows limited performance.

C. Study limitations

This study has several limitations that should be considered when interpreting the results.

First, the IGRF model does not incorporate Solar activity. Thus, Solar-driven disturbances on the Earth's magnetic field are not taken into account in the simulations. As a consequence, short-timescale magnetic field variations caused by solar-driven currents are neglected. This limits the achievable accuracy of satellite simulations, particularly for high-precision attitude determination.

The satellite was modeled as a rigid body for the entirety of this study, including all simulations. In general, applied control torques may excite structural flexible modes, particularly those associated with the solar panels. However, due to the inherently low bandwidth of the B-dot control law, such flexural mode excitation is not expected to be significant.

In addition, this study exclusively examined detumbling performance, whereas operational criteria for ASM mode primarily depend on the ability to point the solar arrays towards the Sun. Consequently, additional research focusing on this aspect would be valuable.

V. CONCLUSION

This study demonstrates that magnetic attitude control in LEO is effective for inclinations as low as 35°, achieving detumbling within less than two orbits. The results highlight inclination as the primary factor influencing detumbling time, with other orbital parameters and initial conditions having comparatively negligible impact. Additionally, the final attitude consistently aligns the axis of maximum inertia (or spin axis) within 45° of the orbit normal. For inclinations above 42°, the convergence time in attitude remains below two orbits. Notably, some simulations in near-equatorial orbits revealed a metastable state, where the system persisted for over a day before transitioning to a lower-energy state. However, some variability in the results could not be fully explained by initial condition variations, as minute changes in initial conditions had great impacts on results, suggesting there might be an underlying chaotic behavior here. Future studies could explore these factors in more detail, potentially involving more advanced modeling or experimental validation.

The ability to use magnetic attitude control in orbits with an inclination as low as 35° offers a robust and reliable solution for spacecraft attitude control, particularly for Cubesat missions. This finding could significantly impact mission design and planning, enabling more flexible and cost-effective spacecraft operations.

APPENDIX

a. Justification of convergence time criteria

Actually, a more simple criteria was first imagined :

$$t_{\text{conv}} \text{ s.t. } \|\varepsilon(t) - \bar{\varepsilon}\| \leq 0.2^\circ/\text{s}, \forall t \geq t_{\text{conv}}$$

meaning that the error converges at the first instant when it is at most $0.2^\circ/\text{s}$ away from its mean value during last orbit. However, this criteria was found to be too strict and presented some limitations. It considered some simulations to converge quite late although it looked like the convergence time should have been much lower. Figure 30 shows the results which were obtained:

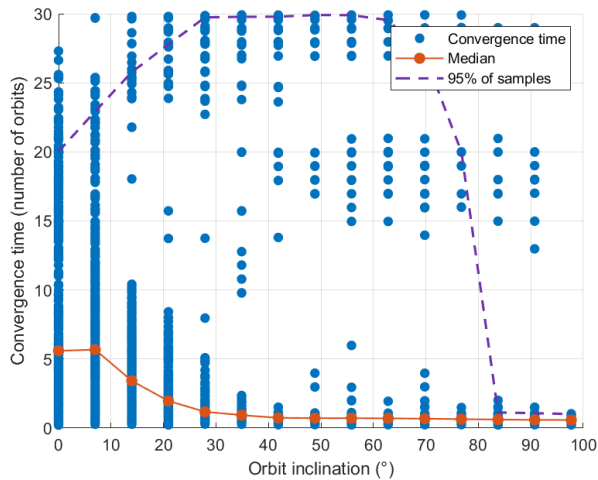


Fig. 30: Convergence time per orbit inclination based on the first criteria

There were a lot of outliers at high inclinations such as the results shown in Figure 31:

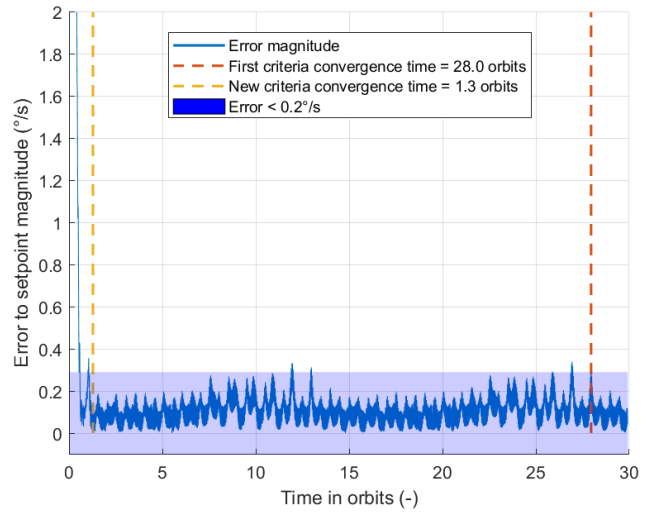


Fig. 31: Comparison of first and new criteria for convergence time computation for simulation 8081

Here, the simulation was almost within the convergence criteria except at a few instants where it barely was out of it. This is why, in the latest version of the criteria, only 90% of the data points need to be within it to have converged. Nevertheless, this created a new issue, where some simulations which converged very quickly now had a convergence time which was during the transient.

Thus, to improve the criteria, the last addition to it was to also track whether the slope of the error was below $0.1^\circ/\text{s}^2$.

b. Justification of equation (13)

Let us develop

$$\mathbf{p} = \mathbf{b} \times (\mathbf{u} \times \mathbf{b})$$

Using the double cross product rule:

$$\mathbf{u} \times (\mathbf{v} \times \mathbf{w}) = (\mathbf{u} \cdot \mathbf{w}) \mathbf{v} - (\mathbf{u} \cdot \mathbf{v}) \mathbf{w}$$

$$\begin{aligned} \mathbf{p} &= (\mathbf{b} \cdot \mathbf{b}) \mathbf{u} - (\mathbf{b} \cdot \mathbf{u}) \mathbf{b} \\ &= \mathbf{u} - (\mathbf{b} \cdot \mathbf{u}) \mathbf{b} \\ &= [\mathbf{I}_3 - \mathbf{b}\mathbf{b}^T] \mathbf{u} \end{aligned}$$

Thus, the application $\mathbf{u} \mapsto \mathbf{b} \times (\mathbf{u} \times \mathbf{b})$ is the orthogonal projector w.r.t. \mathbf{b} .

ACKNOWLEDGMENT

The research presented in this paper was carried out during an internship at CNES.

I would like to thank the AOCS team for their kindness, support and mentorship. I am especially grateful to my supervisors Leo Martinez and Lorenzo Laurent who offered precious guidance and expertise. Also, I would like to express my gratitude to Dr. Gunnar Tibert for his help throughout the research process. Finally, I would like to thank my partner for her invaluable support during this project.

References

- [1] H. Schaub and J. L. Junkins, *Analytical Mechanics of Space Systems*, 4th. Reston, VA: AIAA Education Series, 2018. DOI: 10.2514/4.105210.
- [2] CNES, *Techniques et Technologies des Véhicules Spatiaux - Volume 3 : Plateformes* (Cours de technologie spatiale), 2002nd ed., 3 vols. CNES and CILF, vol. 3.
- [3] G. Avanzini and F. Giuliotti, “Magnetic detumbling of a rigid spacecraft,” *Journal of Guidance, Control, and Dynamics*, vol. 35, no. 4, pp. 1326–1334, Jul. 2012, ISSN: 0731-5090, 1533-3884. DOI: 10.2514/1.53074. Accessed: Sep. 16, 2025. [Online]. Available: <https://arc.aiaa.org/doi/10.2514/1.53074>.
- [4] F. L. Markley and J. L. Crassidis, *Fundamentals of Spacecraft Attitude Determination and Control*. New York, NY: Springer New York, 2014, ISBN: 978-1-4939-0801-1 978-1-4939-0802-8. DOI: 10.1007/978-1-4939-0802-8. Accessed: Sep. 16, 2025. [Online]. Available: <http://link.springer.com/10.1007/978-1-4939-0802-8>.
- [5] M. Y. Ovchinnikov, D. Roldugin, S. Tkachev, and V. Penkov, “B-dot algorithm steady-state motion performance,” *Acta Astronautica*, vol. 146, pp. 66–72, May 2018, ISSN: 00945765. DOI: 10.1016/j.actaastro.2018.02.019. Accessed: Jan. 9, 2026. [Online]. Available: <https://linkinghub.elsevier.com/retrieve/pii/S0094576517317332>.
- [6] CNES, *Techniques et Technologies des Véhicules Spatiaux - Volume 1 : Généralités et contraintes de développement* (Cours de technologie spatiale), 2002nd ed., 3 vols. CNES and CILF, vol. 1.
- [7] D. Roldugin and M. Ovchinnikov, “Explicit solution for the attitude motion of a bias momentum satellite under bdot magnetic damping,” *Aerospace Science and Technology*, vol. 159, p. 110019, Apr. 2025, ISSN: 12709638. DOI: 10.1016/j.ast.2025.110019. Accessed: Jan. 9, 2026. [Online]. Available: <https://linkinghub.elsevier.com/retrieve/pii/S1270963825000914>.